

Frequency-Domain Thermal Modeling and Characterization of Power Semiconductor Devices

Ke Ma, *Member, IEEE*, Ning He, *Student Member, IEEE*, Marco Liserre, *Fellow, IEEE*,
and Frede Blaabjerg, *Fellow, IEEE*

Abstract—The thermal behavior of power electronics devices has been a crucial design consideration, because it is closely related to the reliability and also the cost of the converter system. Unfortunately, the widely used thermal models based on lumps of thermal resistances and capacitances have their limits to correctly predict the device temperatures, especially when considering the thermal grease and heat sink attached to the power semiconductor devices. In this paper, frequency-domain approach is applied to the modeling of the thermal dynamics for power devices. The limits of the existing RC lump-based thermal networks are explained from a point of view of frequency domain. Based on the discovery, a more advanced thermal model developed in the frequency domain is proposed, which can be easily established by characterizing the slope variation from the bode diagram of the typically used Foster thermal network. The proposed model can be used to predict not only the internal temperature behaviors of the devices but also the behaviors of the heat flowing out of the devices. As a result, more correct estimation of device temperature can be achieved when considering the cooling conditions for the devices.

Index Terms—Power electronics, power semiconductor device, thermal model.

I. INTRODUCTION

POWER electronics are being widely used in many important applications of energy conversion system like renewable energy production, motor drives, transportations, and power transmission, where the cost of maintenances and failures might be high. Consequently, the reliability requirements for power electronics in these systems are getting more critical [1]–[4]. Thermal loading of power semiconductors are especially important, as it is one of the most expensive components and dominant heat sources. It has been demonstrated in [5] that the thermal dynamics under various time scales either inside or outside the power semiconductors could contribute to the quantified damage of the component. As stated in [6]–[12], the fast

Manuscript received July 3, 2015; revised October 13, 2015; accepted November 24, 2015. Date of publication December 17, 2015; date of current version May 20, 2016. This work was financially supported by the European Research Council under the European Union’s Seventh Framework Programme/ERC Grant Agreement 616344, and by the Centre of Reliable Power Electronics, Aalborg University, Denmark. Recommended for publication by Associate Editor J. Wang.

K. Ma is with the Energy Technology, Aalborg University, Aalborg DK-9220, Denmark, he is also with Department of Electrical Engineering, Shanghai Jiao Tong University, China (e-mail: kema@et.aau.dk).

F. Blaabjerg is with the Energy Technology, Aalborg University, Aalborg DK-9220, Denmark (e-mail: fbl@et.aau.dk).

N. He is with the College of Electrical Engineering, Zhejiang University, Hangzhou zhejiang 310027, China (e-mail: hening722@zju.edu.cn).

M. Liserre is with the Kiel University, Kiel 24118, Germany (e-mail: liserre@ieee.org).

Color versions of one or more of the figures in this paper are available online at <http://ieeexplore.ieee.org>.

Digital Object Identifier 10.1109/TPEL.2015.2509506

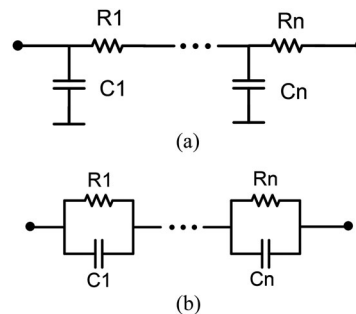


Fig. 1. Commonly used thermal networks for power device based on RC lumps. (a) Cauer type, (b) Foster type.

thermal cycling inside the power devices may cause important fatigues like bond-wire lift-off and cracks/voids in the chip soldering layer, while the slower thermal variations outside the device (i.e., on the case/base plate of device or heat sink) will cause important fatigues like cracks on the soldering layer and the thermal grease. As a result, the accurate temperatures estimation, including the thermal dynamics either inside or outside the power device are critical information, not only for the reliability enhancement but also for the cost-efficient thermal management of the power converter.

Unfortunately, the thermal stress of the power device is a challenge to model, because it is not only related to the characteristic of the device itself, but also depends a lot on the performance of the attached thermal grease and heat sink. Generally, the thermal behavior for the power devices can be modeled by a series of lumps of thermal resistance R and capacitance C [13]–[17], which together are referred as the thermal impedance Z . According to the connection of RC lumps, they can be grouped into Foster or Cauer-type thermal networks, as shown in Fig. 1. The Cauer RC network based on the physical structure of the device is considered to be a relatively correct model to describe the thermal behaviors of power devices. However, an accurate Cauer model is normally hard to use because the internal geometry, materials, and effective heat path of device have to be all determined with the help of Finite Element Method (FEM) simulation. On the other hand, the other RC network named Foster type is more popularly used, because it is based on the measurement of temperature dynamics of power devices [15], [17], and is independent of the internal structure or material.

One problem with the Foster-type thermal network is that its parameters are based on mathematical fitting of the measured/simulated temperature curves, and each of the RC lump in the Foster network represents no physical meaning. Therefore, by using this model, only the overall temperature behaviors

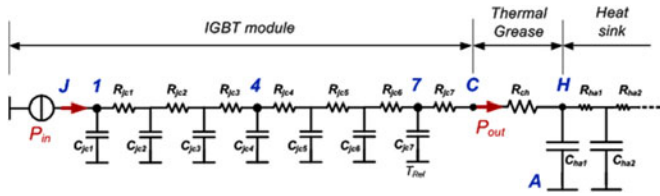


Fig. 2. Cauer-type thermal network based on Fig. 3 as reference of study.

between the measured points can be guaranteed, provided with a known temperature at the node where heat is flowing out [15]. It has been found that when extending the Foster-type thermal network with the thermal models for the thermal grease and heat sink, unrealistic temperature behaviors either inside or outside the power devices will be experienced [13]–[17]. These drawbacks make the Foster-type thermal model hard to be utilized for thermal design or lifetime prediction, where the external temperature and cooling conditions of the power devices need to be carefully characterized.

In order to improve this problem of Foster thermal network, a mathematical transformation is developed which can convert the Foster network to an equivalent Cauer-type with the same number of RC lumps [18], [19]. Although the obvious error of the device temperature when including the cooling conditions seems to be avoided, this mathematical transformation does not regain any physical means of the internal structure of power device, and the accuracy of the estimated device temperature still need to be evaluated.

In the last decade, some more advanced modeling techniques have been introduced to improve the prediction of thermal dynamics for power device [19]–[22]. However, they mainly focus on the internal temperature behaviors of the device, and the problems of the existing thermal models when considering the external cooling conditions are not considered or solved.

In this paper, the power-loss/heat and temperatures of the power semiconductor devices are considered as signals in the frequency domain, and the corresponding frequency-domain models are first established for several typically used thermal networks. Afterwards, the performance and limits of the Foster type and its equivalent Cauer-type thermal model are explained from a new point of view. Based on the discovery, a new thermal model is proposed which put more efforts to establish a correct transfer function for the filtering of the power-loss, and thereby, it can overcome some of the limits in the existing RC thermal networks for the power devices. Finally, some simulation and experimental results are given to validate the accuracy and advantage of the proposal thermal model under both time and frequency domains.

II. FREQUENCY-DOMAIN THERMAL MODELING AND LIMITS OF THE EXISTING THERMAL MODELS BASED ON RC LUMPS

A multilayer Cauer-type thermal network for an IGBT module is first defined as a study reference in this paper, as shown in Fig. 2. This Cauer thermal model is extracted from the internal structure and material specifications for a 1700V/100A IGBT module used for wind power application, as shown in Fig. 3 and

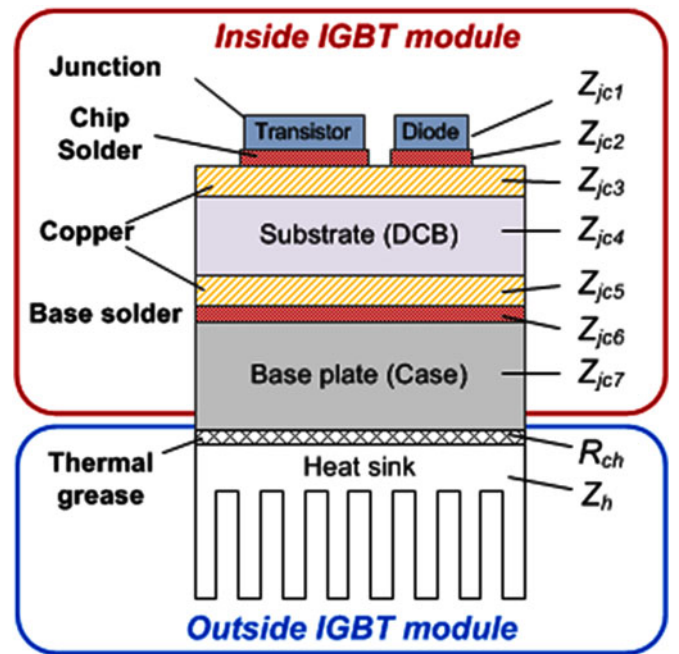


Fig. 3. Construction of an IGBT module as reference for study.

Table I, a heat spreading angle of 45° is assumed in this case. It can be seen that seven Cauer-type RC lumps are introduced to represent seven layers of the internal materials of the device as indicated in Fig. 2. In respect to the cooling conditions outside the device, a large thermal resistance is used to represent the thermal behavior of the thermal grease, and a series of small thermal resistances with large thermal capacitances are used to represent the thermal behavior of the heat sink. It is assumed that the network in Fig. 2 and the parameters in Table I can correctly reflect the temperature behaviors of the given IGBT module under the given specifications and cooling conditions. Although, more detail and complicated modeling techniques, such as [21] and [22] can be introduced to refine the parameters in Table I, they can be updated depending on the needs of accuracy, but they are not considered in this paper.

Inspired by the typical approach used for the analysis of electrical RC circuits, it is also possible to model the frequency-domain characteristics of the thermal RC networks in order to further understand the thermal behaviors and thermal dynamics of the power device, which will be detailed as follows:

A. Thermal Modeling Under Frequency Domain—With Cauer Network as Reference

Normally the power-loss P_{in} is injected into the J or 1 node of the Cauer-type thermal network in Fig. 2, and a series of temperatures and heat flow can be identified in this network. It is noted that the power-loss or heat source P_{in} , which is generated in the chips of the IGBT module, can be seen as a disturbance signal; while the corresponding temperatures on each node of the thermal network or different layers of the material can be seen as response signals, so well as for the heat flowing after each node/layer. As a result, the gain from the disturbance P_{in}

TABLE I
 PARAMETERS FOR THE MATERIAL, LAYER, AND THERMAL IMPEDANCE OF FIG. 3

Layers	Thickness (mm)	Density (g/cm ³)	Specific heat (J/kg °C)	Thermal conductivity (W/m °C)	Thermal resistance (K/W)	Thermal capacitance (J/K)
Chip (Silicon)	0.3	2.3	790	83.6	0.0194	0.1021
Chip solder	0.05	9.7	260	78	0.0034	0.0179
Copper	0.3	8.9	397	386	0.0040	0.2092
DCB (Al ₂ O ₃)	0.7	3.7	880	18	0.1732	0.5118
Copper	0.3	8.9	397	386	0.0030	0.2732
Base solder	0.1	9.7	260	78	0.0048	0.0517
Base (Copper)	3	8.9	397	386	0.0209	4.0898
Thermal grease	0.021	2.25	NA	0.8	0.0518	NA

to each of the thermal response under Laplace domain can be analytically solved with the information of R and C parameters.

One group of important relationships between the thermal disturbance and responses is the gain from input heat P_{in} to the temperature responses on each node of Fig. 2. These gains can be solved by the following functions:

$$Z_{P_{in}T_{X-H}}^{Ref}(s) = \frac{T_X(s) - T_H(s)}{P_{in}}$$

$$= \begin{cases} 1/(\frac{1}{R_{ch} + R_{jcX}} + s \cdot C_{jcX}) & \text{if } X = 7 \\ 1/(\frac{1}{Z_{P_{in}T_{X+1-H}}^{Ref}(s) + R_{jcX}} + s \cdot C_{jcX}) & \text{if } X = 1 \text{ to } 6 \end{cases} \quad (1)$$

where s is the Laplace operator, $Z_{P_{in}T_{X-H}}^{Ref}(s)$ represents the impedance from input loss (P_{in}) to the temperature difference between node X and the heat-sink node H (T_{XH}), when the referenced Cauer network (Ref) is analyzed. R_{ch} is the thermal resistance of thermal grease, R_{jcX} represents the thermal resistance of each of the seven layers inside the IGBT module, and C_{jcX} is the thermal capacitance for each layer. The detailed parameters of R_{ch} , C_{jcX} , and R_{jcX} can be found from Table I. It is noted that for simplicity of analysis, the heat sink temperature T_H is considered as a reference temperature in the modeling process of this paper, because normally the thermal capacitance of suitable heat sink is a factor of 100–1000 compared to the internal thermal capacitance of power device; and the temperature on node H is much more stable than the temperatures on nodes 1 to C. However, other reference node such as ambient A can be chosen as the reference temperature, coming with some small deviations in function (1).

Another group of important relationships between the thermal disturbance and responses are the gains from input heat P_{in} to the heat flowing out of each node in Fig. 2. This group of relationships typically is not considered in most of the existing thermal networks, and can be solved as the following functions for the reference Cauer model: (2) shown at bottom of the page. where $G_{P_{in}P_X}^{Ref}(s)$ represents the gain from input heat/loss (P_{in})

to the heat flowing out of node X (P_X), when the reference Cauer network (Ref) is chosen.

Based on (1) and (2), the gain from P_{in} to the temperature difference between junction node J and case node C , as well as the gains from P_{in} to the heat flowing out of the device P_{out} , can be solved as

$$Z_{P_{in}T_{jc}}^{Ref}(s) = \frac{T_{j-H}(s) - T_{c-H}(s)}{P_{in}}$$

$$= Z_{P_{in}T_{1-H}}^{Ref}(s) - R_{ch} \cdot G_{P_{in}P_7}^{Ref}(s) \quad (3)$$

$$G_{P_{in}P_{out}}^{Ref}(s) = G_{P_{in}P_7}^{Ref}(s). \quad (4)$$

It is noted that $G_{P_{in}T_{jc}}$ and $G_{P_{in}P_{out}}$ are selected as two of the indicators to benchmark the accuracy of thermal models focused in this paper. As a result the frequency-domain model for the reference seven-layers Cauer-type thermal network is established.

B. Thermal Modeling Under Frequency Domain—Foster Network

When applying a step power-loss P_{in} to the reference Cauer network shown in Fig. 2, the temperature response in node J and C can be measured and recorded, afterwards the Foster-type thermal network, and its RC parameters can be extracted by curve-fitting the time-domain temperature responses with the following functions [10]:

$$Z_{jc}^{Foster}(t) = \frac{T_j(t) - T_c(t)}{P_{in}} = \sum_{n=1}^X R_{fn} \cdot (1 - e^{-t/(R_{fn} \cdot C_{fn})}) \quad (5)$$

where R_{fn} and C_{fn} represent the mathematically-solved thermal resistance and thermal capacitance for the Foster thermal network, and are connected in the form as indicated in Fig. 4. In (5) X means the number of pairs for the used R_{fn} and C_{fn} , normally four pairs of the Foster RC parameters can achieve an accurate fitting to most of the temperature responses between nodes J

$$G_{P_{in}P_X}^{Ref}(s) = \begin{cases} \frac{G_{P_{in}P_{X+1}}^{Ref}(s)}{R_{ch} + R_{jcX}} / (\frac{1}{R_{ch} + R_{jcX}} + s \cdot C_{jcX}), & \text{if } X = 7 \\ \frac{G_{P_{in}P_{X-1}}^{Ref}(s)}{G_{P_{in}T_{X+1-H}}^{Ref}(s) + R_{jcX}} / (\frac{1}{G_{P_{in}T_{X+1-H}}(s) + R_{jcX}} + s \cdot C_{jcX}), & \text{if } X = 1 - 6 \end{cases} \quad (2)$$

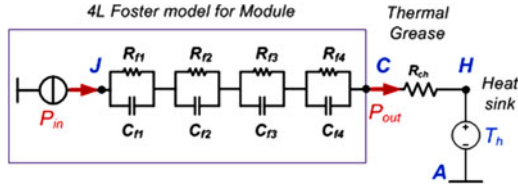


Fig. 4. Foster-type 4L thermal network fitted from the referenced Cauer network shown in Fig. 2. (J denotes junction node, C denotes case node, H denotes heat-sink node, A denotes ambient node).

TABLE II
RC PARAMETERS OF THE FOSTER AND EQUIVALENT CAUER NETWORK IN FIGS. 4 AND 5

Foster network		Equivalent Cauer network	
Thermal resistance Rf1-4 (W/K)	Thermal capacitance Cf1-4 (J/K)	Thermal resistance Rec1-4 (W/K)	Thermal capacitance Cec1-4 (J/K)
0.0014	15.646	0.0249	0.1062
0.0188	0.0023	0.1602	0.7285
0.0892	0.4059	0.0422	8.39
0.1191	0.1167	0.0013	11950

and C for the IGBT module. In this paper, the RC parameters are summarized in Table II.

The gain from input loss P_{in} to the temperature difference between node X and heat sink, as well as the gain from input loss P_{in} to the heat flow/power-loss after each node X can be solved in (6) and (7), respectively, for the Foster thermal network as

$$Z_{P_{in} T_{X-H}}^{Foster}(s) = \sum_{n=X}^4 \frac{R_{fn}}{R_{fn} C_{fn} \cdot s + 1} + R_{ch} \quad (6)$$

$$G_{P_{in} P_{out}}^{Foster}(s) = 1. \quad (7)$$

Then the two benchmark indicators $Z_{P_{in} T_{jc}}$ and $G_{P_{in} P_{out}}$ for the given four-layers Foster thermal network can be solved in

$$Z_{P_{in} T_{jc}}^{Foster}(s) = \sum_{n=1}^4 \frac{R_{fn}}{R_{fn} C_{fn} \cdot s + 1} \quad (8)$$

$$G_{P_{in} P_{out}}^{Foster}(s) = 1. \quad (9)$$

C. Thermal Modeling in the Frequency Domain—Equivalent Cauer Network [18]

This type of thermal network targets to solve some problems of the Foster-type thermal network as aforementioned, and it is often used for the electro-thermal simulation of the power device temperature. By applying the mathematical transformation and boundary conditions shown in [18], the Foster-type RC network in Fig. 4 can be converted to an equivalent Cauer-type thermal network with the same pair numbers of RC parameters but different values, as shown in Fig. 5 and Table II.

Thereby, the frequency-domain thermal model for the given four-layers equivalent Cauer RC network can be established. The gain from input loss P_{in} to the temperature difference between node X and heat sink, as well as the gain from input loss P_{in}

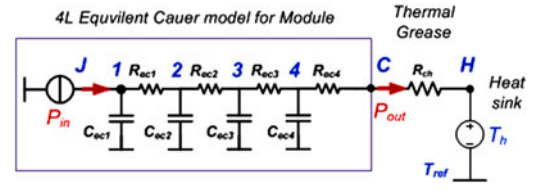


Fig. 5. Equivalent 4L Cauer-type thermal network converted from the Foster network shown in Fig. 4. (J denotes junction node, C denotes case node, H denotes heat-sink node, A denotes ambient node).

to the heat-flow/power-loss after each node X can be solved in (10), and (11) shown at bottom of the next page, respectively. The two benchmark indicators $Z_{P_{in} T_{jc}}$ and $G_{P_{in} P_{out}}$ can be solved in (12) and (13):

$$Z_{P_{in} T_{X-H}}^{eqCauer}(s) = \frac{T_X - T_H}{P_{in}} = \begin{cases} 1 / \left(\frac{1}{R_{ch} + R_{ecX}} + s \cdot C_{ecX} \right), & \text{if } X = 4 \\ 1 / \left(\frac{1}{Z_{P_{in} T_{X+1-H}}^{eqCauer}(s) + R_{ecX}} + s \cdot C_{ecX} \right), & \text{if } X = 1 \text{ to } 3 \end{cases} \quad (10)$$

$$Z_{P_{in} T_{jc}}^{eqCauer}(s) = \frac{T_{j-H} - T_{c-H}}{P_{in}} = Z_{P_{in} T_{1-H}}^{eqCauer}(s) - R_{ch} \cdot G_{P_{in} P_4}^{eqCauer}(s) \quad (12)$$

$$G_{P_{in} P_{out}}^{eqCauer}(s) = G_{P_{in} P_7}^{eqCauer}(s). \quad (13)$$

D. Limits of the Existing Thermal Models Based on RC Lumps

With the built frequency-domain models of the three types of thermal networks, the Bode plot of some interesting gains can be compared. One benchmark Bode plot is the gain from loss P_{in} to the temperature difference between junction and case, which is normally provided by the manufacturer datasheet or measured by the user as an important thermal characteristic of the power device. As it can be seen in Fig. 6(a), the difference in gains among the three types of thermal models is almost ignorable.

However, when comparing the Bode plot of the other benchmark gains from P_{in} to the output heat of power device P_{out} , the difference among the three types of thermal models are significant, as shown in Fig. 6(b): As the correct thermal behavior assumed in this paper, the reference seven-layers Cauer-type thermal network (Cauer_ref) behaves like a second-order low-pass filter (LPF) to the input heat P_{in} with bandwidth around 0.5 Hz. The curve-fitted four-layers Foster-type thermal network (Foster_4L) behaves transparently to the frequency components of P_{in} , whose disturbances will be immediately seen by the thermal grease and heat sink outside the power device (obviously incorrect in real case). On the contrary the equivalent four-layers Cauer-type thermal network (eqCauer_4L) transformed from Foster_4L has much lower bandwidth compared to the Cauer_Ref, which means many important disturbances of P_{in} in the real case will be blocked and not seen by the thermal grease and heat sink.

By including a large thermal resistance R_{ch} of the thermal grease to the three thermal networks, the Bode plot of the gains from P_{in} to the junction temperature T_j with different thermal

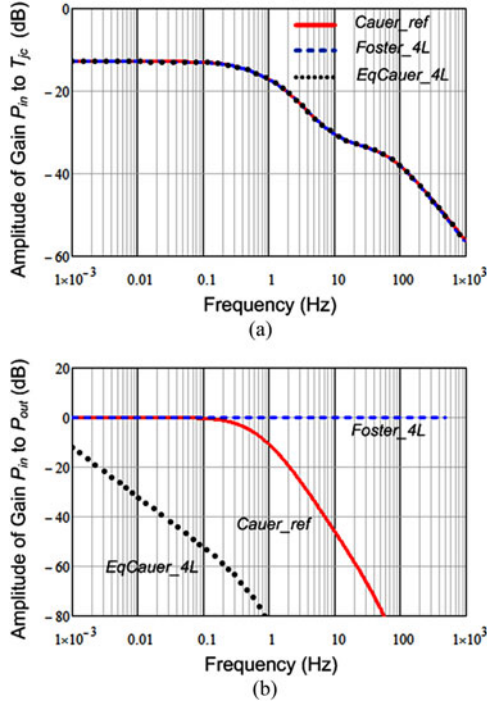


Fig. 6. Bode plot of critical gains in various thermal networks under frequency domain. (Cauer_ref: reference seven-layer Cauer thermal network, Foster_4L: four-layer Foster-type fitting network to the temperature response of Cauer_ref, EqCauer_4L: mathematical transformation from Foster_4L to the equivalent Cauer type). (a) Gains from P_{in} to T_{jc} (b) Gains from P_{in} to P_{out} .

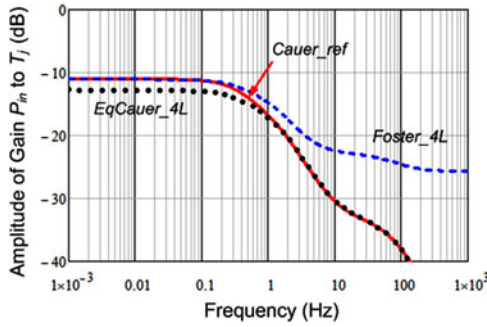


Fig. 7. Bode plot of gains from P_{in} to T_j in various thermal networks. (Heat-sink temperature T_H is used as reference temperature, Cauer_ref: reference seven-layer Cauer-type thermal network, Foster_4L: four-layer Foster-type fitting network to the temperature response of Cauer_Ref network, EqCauer_4L: mathematical transformation from Foster_4L to the equivalent Cauer type).

networks are shown in Fig. 7, (with heat-sink temperature T_H as the reference temperature). It can be seen that the limits of the Foster_4L and eqCauer_4L thermal network can be more clearly identified: The Foster_4L has a good agreement with the reference Cauer model at lower frequency band, but there is a large error on the high-frequency band. On the contrary, the eqCauer_4L has a good agreement with the reference Cauer

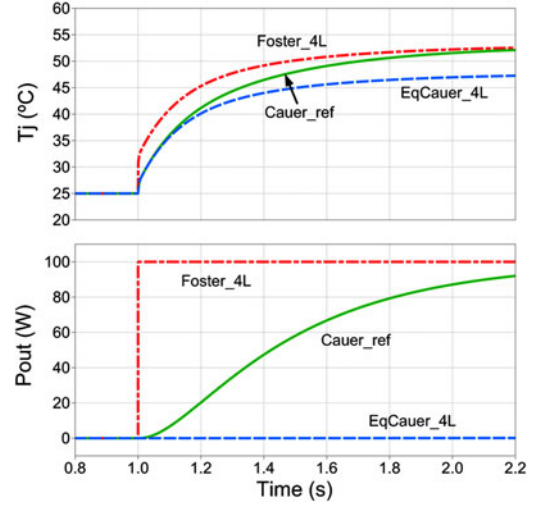


Fig. 8. Time-domain simulation of the junction temperature under a step power-loss in various thermal networks (100-W loss step at 1 s, $T_H = 25^\circ\text{C}$).

model at high-frequency band, but there is a large error at the low-frequency band.

The time-domain simulations also agree with the behaviors predicted in the frequency domain, as shown in Fig. 8, where a step power-loss P_{in} of 100 W at the time of 1 s is applied to various thermal networks. It can be seen that compared to the Cauer_Ref model, the Foster network has no filtering effect to the injected power-loss/heat, which immediately flows through the thermal grease outside the device, and results in a large error at the beginning of the thermal transient of the junction temperature T_j ; but the steady-state T_j is more consistent with the Cauer_Ref. The equivalent Cauer-type network converted from the Foster type has an overfiltering effect to the injected power-loss/heat, and thereby the junction temperature T_j has a large error at the steady-state, but it has good agreement at the beginning of the thermal transient with the Cauer_Ref.

As a conclusion, either the Foster or its equivalent Cauer-type thermal network has their limits to describe the correct thermal dynamics of the power device. The key to achieve more correct thermal modeling, especially when considering the thermal grease and heat sink, is to create a correct filtering to the power-loss—or correct heat-gain from P_{in} to P_{out} ($G_{P_{in}P_{out}}$) under the frequency domain.

III. NEW THERMAL MODEL FOR POWER DEVICE UNDER FREQUENCY DOMAIN

A. Characterization of the Heat Flowing Out of Device

In the practice, the Cauer-type RC parameters based on the structure and material of the power semiconductor devices is difficult to be accurately accessed; and the correct heat-gain

$$G_{P_{in}P_X}^{\text{eqCauer}}(s) = \begin{cases} \frac{G_{P_{in}P_{X-1}}^{\text{eqCauer}}(s)}{R_{ch} + R_{ecX}} / \left(\frac{1}{R_{ch} + R_{ecX}} + s \cdot C_{ecX} \right), & \text{if } X = 4 \\ \frac{G_{P_{in}P_{X-1}}^{\text{eqCauer}}(s)}{G_{P_{in}T_{X+1-H}}^{\text{eqCauer}}(s) + R_{ecX}} / \left(\frac{1}{G_{P_{in}T_{X+1-H}}^{\text{eqCauer}}(s) + R_{ecX}} + s \cdot C_{ecX} \right), & \text{if } X = 1 \text{ to } 3 \end{cases} \quad (11)$$

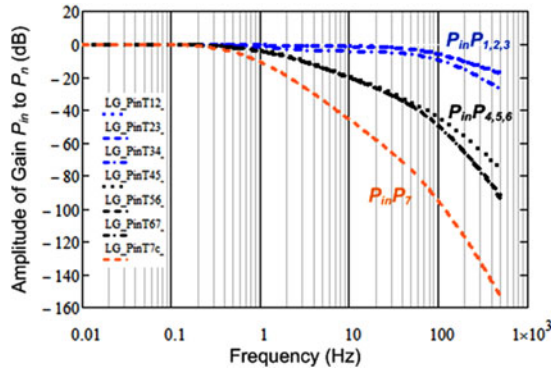


Fig. 9. Bode plot of heat-gains in different nodes of the reference seven-layers Cauer network.

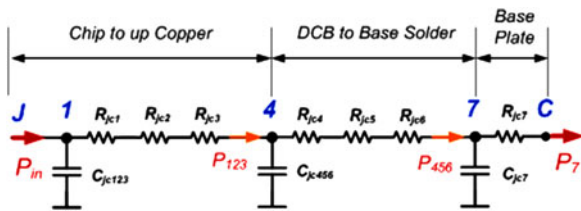


Fig. 10. Transforming of the 7L-Cauer-type network to three cascaded LPF according to the frequency behaviors of Fig. 9.

from P_{in} to P_{out} is also hard to be directly solved from the commonly used Foster-type thermal network. Thereby, other approaches have to be investigated in order to find the correct gain from P_{in} to P_{out} .

As illustrated in Fig. 9, by looking at the slopes and corner frequencies of the heat-gains $G_{P_{in}P_1}$ to $G_{P_{in}P_7}$, the seven layers of materials in the reference Cauer network can be generally seen as a series of LPFs, and can be classified into three dominant groups: The first group consists of layers from chip to the upper copper as shown in Fig. 10, (see Nodes 1–4 in Fig. 2), the second group consists of layers from DCB to Base solder (Nodes 4–7), and the third group consists of layer of base plate (Nodes 7–C). It is interesting to see that in each group of material layers, the frequency behaviors of heat-gains are very similar to each other. The characteristics (corner frequencies and slope changes) among the three groups of heat-gains generally follow the behaviors of three cascaded LPFs. As a result, the reference seven-layer Cauer-type thermal network for the device can be degraded to three-cascaded first-order LPFs, as illustrated in Fig. 10, where C_{jc123} , C_{jc456} , C_{jc7} represent the virtual thermal capacitances for each dominant group of layers, and P_{123} , P_{456} , P_7 represent the virtual heat flowing out of each dominant group of layers.

Because the DC gains of the heat transfer function on each node all equal to 0 dB, the key to establish correct gain from input loss P_{in} to output loss of device P_{out} ($G_{P_{in}P_{out}}$), is to identify the three dominant corner-frequencies of the cascade LPF shown in Fig. 9.

Based on the simplified thermal network shown in Fig. 10, the benchmark thermal impedance of the power device $Z_{P_{in}T_{jc}}$

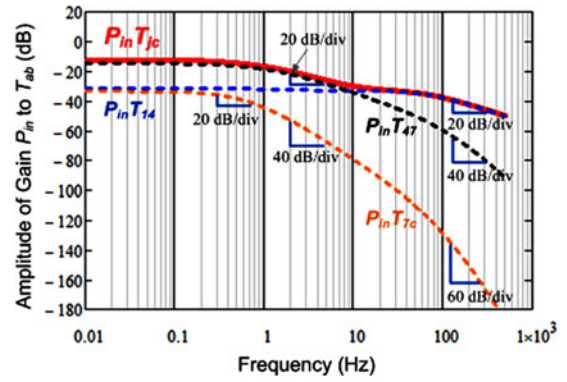


Fig. 11. Bode plot and slope of thermal impedance gains for the reference 7L Cauer-type network.

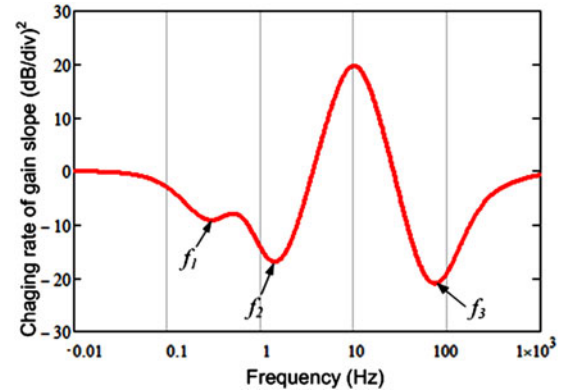


Fig. 12. Identified corner-frequencies from bode plot of $Z_{P_{in}T_{jc}}$ in Fig. 11.

can be revised as the sum of three parts

$$\begin{aligned} Z_{P_{in}T_{jc}}(s) &= Z_{P_{in}T_{j4}}(s) + Z_{P_{in}T_{47}}(s) + Z_{P_{in}T_{7c}}(s) \\ &= G_{P_{in}P_{123}}(s) \cdot \sum_{X=1}^3 R_{jcX} + G_{P_{in}P_{456}}(s) \\ &\quad \cdot \sum_{X=4}^6 R_{jcX} + G_{P_{in}P_7}(s) \cdot R_{jc7}. \end{aligned} \quad (14)$$

By ignoring some of the high frequency band behaviors in the heat-gains $G_{P_{in}P_{456}}$, $G_{P_{in}P_7}$, and only considering their first-order low-pass filter behaviors, (14) can be simplified as

$$\begin{aligned} Z_{P_{in}T_{jc}}(s) &\approx G_{P_{in}P_{123}}(s) \cdot R_{jc1-3} + G_{P_{123}P_{456}}(s) \\ &\quad \cdot R_{jc4-6} + G_{P_{456}P_7}(s) \cdot R_{jc7} \\ &= \frac{1}{\frac{1}{2\pi f_{cr1}} \cdot s + 1} \cdot R_{jc1-3} + \frac{1}{\frac{1}{2\pi f_{cr2}} \cdot s + 1} \\ &\quad \cdot R_{jc4-6} + \frac{1}{\frac{1}{2\pi f_{cr3}} \cdot s + 1} \cdot R_{jc7} \end{aligned} \quad (15)$$

which is equivalent to the form of three-layers Foster thermal network under frequency-domain, and the frequencies f_{crX} on each layer of the Foster network is the same as the corner frequencies in the heat-gains.

It can be seen that the thermal impedance $Z_{P_{in}T_{jc}}$ is inherently correlated with the heat-gains of the three dominant

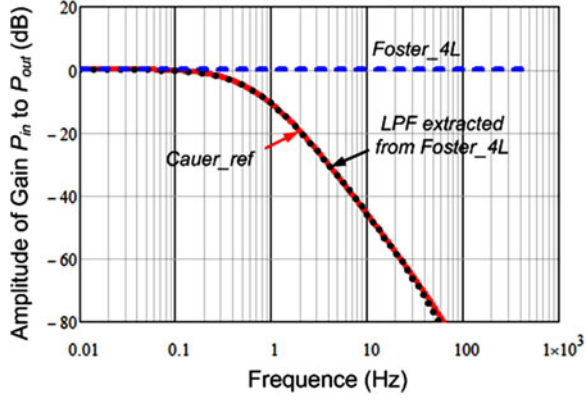
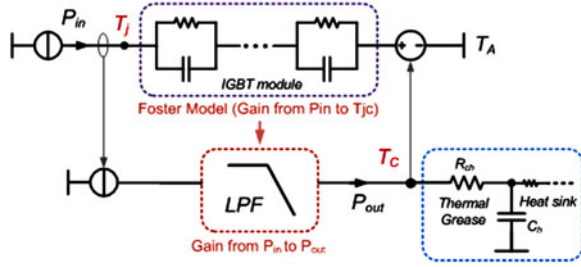

 Fig. 13. Bode plot of heat-gain $G_{P_{in}P_{out}}$ by different thermal networks.


Fig. 14. Proposed thermal model for power device based on frequency domain.

groups of material. Therefore, it is possible to extract the corner-frequencies of the heat-gains from the thermal impedance $Z_{P_{in}T_{jc}}$, which can be more accurately and easily acquired with experimental measurement. Then, the key of the question is to determine the correct values of corner frequencies and thermal resistance on each layer of (15), by knowing the behaviors of $Z_{P_{in}T_{jc}}(t)$.

In Fig. 11, the Bode diagram of $Z_{P_{in}T_{jc}}(s)$ and its three components $Z_{P_{in}T_{14}}$, $Z_{P_{in}T_{47}}$, and $Z_{P_{in}T_{7C}}$ are plotted with the slope changing information, several corner-frequencies on $Z_{P_{in}T_{14}}$, $Z_{P_{in}T_{47}}$, and $Z_{P_{in}T_{7C}}$ can be seen. By applying a deviating operator $F(x)$ to the $Z_{P_{in}T_{jc}}(s)$, as illustrated in (16), the slope deviation on the amplitude of the $Z_{P_{in}T_{jc}}(s)$ can be identified, as shown in Fig. 12, in which the turning points (representing several critical frequencies f_1-f_3) are closely related to the corner frequencies $f_{cr1}-f_{cr3}$ on the three groups of heat-gains in Fig. 9

$$F(x) = \frac{d^2}{dx^2} 20 \times \log_{10} (|Z_{P_{in}T_{jc}}(x)|) \quad (16)$$

(The transfer function $Z_{P_{in}T_{jc}}(s)$ is first converted to the function of frequency f as $Z_{P_{in}T_{jc}}(f)$ by replacing s with $2\pi f \cdot j$, and then $Z_{P_{in}T_{jc}}(f)$ is converted to a function of intermedia variable x as $Z_{P_{in}T_{jc}}(x)$ by replacing f with 10^x).

However, according (15), the critical-frequencies identified from $Z_{P_{in}T_{jc}}$ are slightly different from the corner-frequencies in the heat-gains, because the corner-frequencies in the heat-gains will be disturbed during the weighted summing up with R_{jcX} to compose $Z_{P_{in}T_{jc}}$.

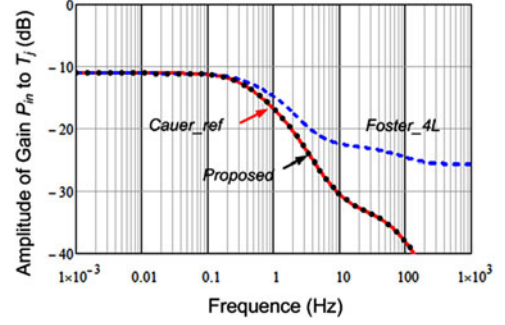
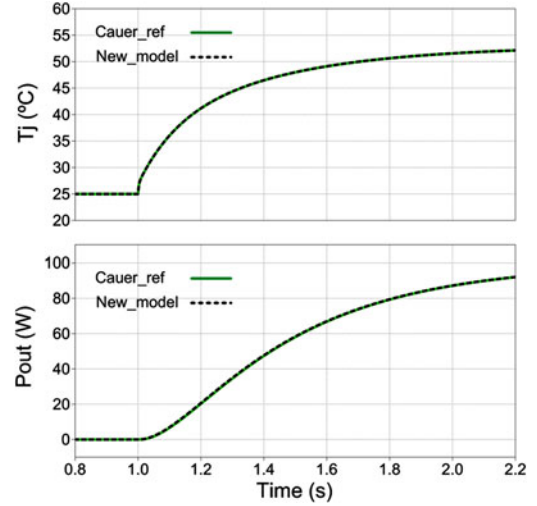

 Fig. 15. Bode plot of gains from P_{in} to T_j in various thermal networks. (T_H is used as a reference temperature).


Fig. 16. Time-domain simulation of the thermal dynamics under a step power-loss in the proposed thermal network (same conditions of Fig. 8, 100 W loss step at 1 s).

One solution to this problem is to refit $Z_{P_{in}T_{jc}}(t)$ with a new Foster network, by setting the boundary conditions of fitting algorithm with the numbers and ranges of critical frequencies f_1-f_3 identified from Fig. 12. As a result the parameters in each layer of (15) can be solved, which includes the information of critical frequencies $f_{cr1}-f_{cr3}$ in the heat-gains. It is noted that the number of Foster layers used for refitting depends on the number of critical frequency identified from $Z_{P_{in}T_{jc}}(s)$. In the case of the given IGBT module for case study, three critical frequencies $f_1 = 0.316$, $f_2 = 1.422$, and $f_3 = 74.129$ Hz can be identified from $Z_{P_{in}T_{jc}}(s)$ as boundary conditions for fitting, and three frequencies of $f_{cr1} = 0.38$, $f_{cr2} = 1.36$, and $f_{cr3} = 70.36$ Hz, can be solved from the fitted Foster network as the corner frequencies for heat-gains.

By cascading the three first-order LPFs with the extracted corner frequencies and unity DC gain, the heat-transfer function $G_{P_{in}P_{out}}$ for the power device can be recomposed by only the information of the measured Foster-type thermal impedance $Z_{P_{in}T_{jc}}$. So the LPF for the power-loss can be calculated as

$$G_{LPF}(s) = \frac{2\pi f_{cr1}}{s + 2\pi f_{cr1}} \cdot \frac{2\pi f_{cr2}}{s + 2\pi f_{cr2}} \cdot \frac{2\pi f_{cr3}}{s + 2\pi f_{cr3}} \quad (17)$$

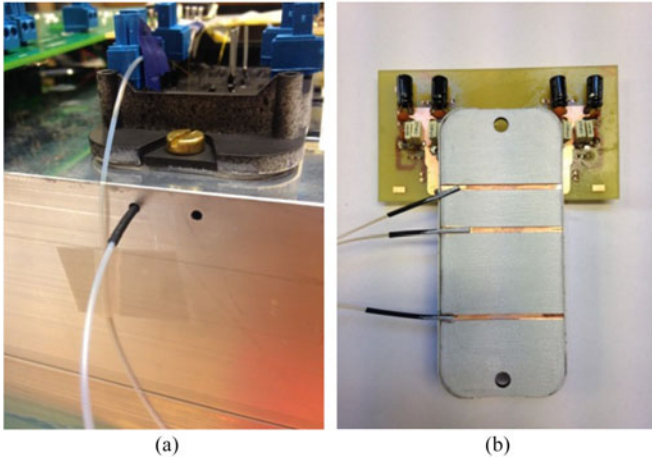


Fig. 17. Experimental setup and sensor locations for the thermal measurements of power device. (a) Sensors attached in the base plate of device. (b) Sensors attached in the heat sink.

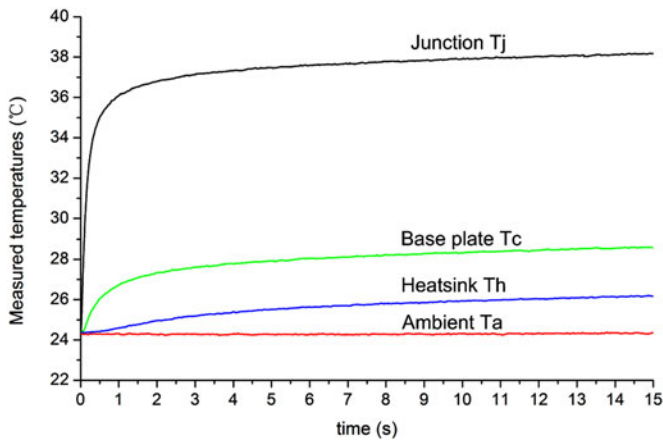


Fig. 18. Measured thermal dynamics under a step power-loss of 26.3 W in a IGBT chip.

In Fig. 13, the Bode plot of the heat-gains $G_{P_{in}P_{out}}$ by the new methods are shown, and it can be seen that the extracted third-order LPF from the Foster thermal network has almost the same frequency behavior with the $G_{P_{in}P_{out}}$ in the reference Cauer thermal network. As a comparison, the $G_{P_{in}P_{out}}$ of the Foster thermal network in Fig. 4 is also shown.

B. New Thermal Model in the Frequency Domain

As a result, a new thermal model is proposed based on the extracted $G_{P_{in}P_{out}}$. As shown in Fig. 14, the proposed thermal model contains of two paths: The first thermal path is used for the junction-temperature estimation inside power device. In this path, the datasheet-based or experimentally measured Foster thermal networks of power device are used, and only a reference temperature, whose value is determined by the case temperature T_C from the other thermal path, is connected. The second thermal path is used for the temperature estimation outside device. In this path the extracted LPF from the Foster thermal network is used to model the loss behaviors flowing out of the device, and the filtered loss can create correct temperature behavior of thermal grease T_{CH} and heat sink T_{HA} outside the devices.

TABLE III
EXTRACTED PARAMETERS OF THE FOSTER AND EQUIVALENT CAUER NETWORK FROM THE EXPERIMENTAL RESULTS

Foster network		Equivalent Cauer network	
Thermal resistance Rf1-3 (W/K)	Thermal capacitance Cf1-3 (J/K)	Thermal resistance Rec1-3 (W/K)	Thermal capacitance Cec-3 (J/K)
0.0219	46.6	0.3466	0.3713
0.2019	0.631	0.01655	60.43
0.1395	0.920	0.000196	661.9

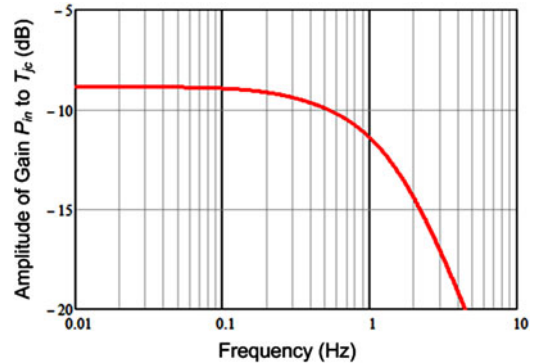


Fig. 19. Bode plot of the measured thermal impedance from P_{in} to T_{jc} ($Z_{P_{in}T_{jc}}$).

The two benchmark indicators $Z_{P_{in}T_{jc}}$ and $G_{P_{in}P_{out}}$ for the new thermal model can be solved in (18) and (19), and then the gain from P_{in} to junction temperature can be calculated in (20)

$$G_{P_{in}T_{jc}}^{New}(s) = G_{P_{in}T_{jc}}^{Foster}(s) \quad (18)$$

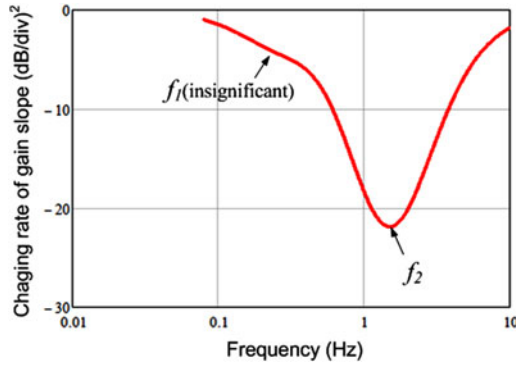
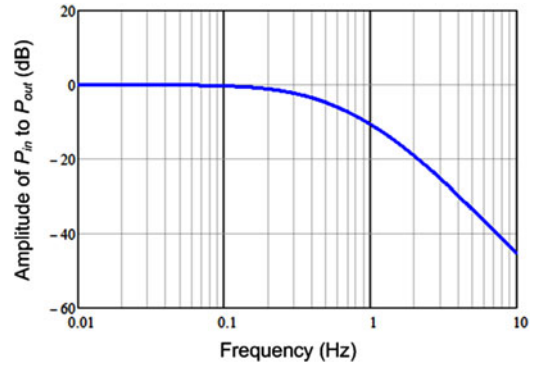
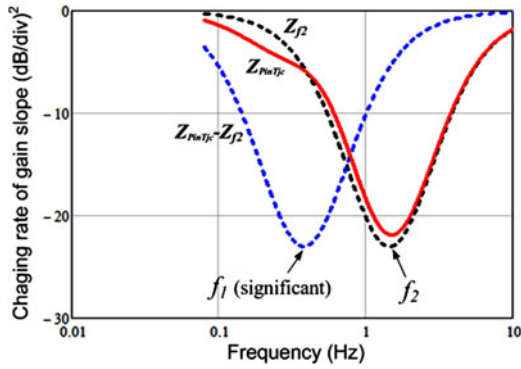
$$G_{P_{in}P_{out}}^{New}(s) = G_{LFP}(s) \quad (19)$$

$$\begin{aligned} Z_{P_{in}T_j}^{New}(s) &= \frac{T_{jc} + T_{ch}}{P_{in}} \\ &= Z_{P_{in}T_{jc}}^{Foster}(s) + R_{ch} \cdot G_{LFP}(s). \end{aligned} \quad (20)$$

The Bode plot of $Z_{P_{in}T_j}$ and the time-domain simulation on the same conditions of Fig. 8 are implemented on the new thermal model, as shown in Figs. 15 and 16, respectively. It can be seen that, there are good agreement of the new thermal model with the reference seven-layer Cauer model both in the frequency domain and in the time domain. It is noted that the new thermal model is only based on the information of Foster-type thermal network, which is commonly accessed from the datasheet or external measurements of device, and it is independent of the internal materials, structure, and heat-path information of devices, being a promising advantage.

IV. EXPERIMENTAL CHARACTERIZATION AND VALIDATION

A 30-A/1200-V power Module for PV application is used to validate the performance of the proposal thermal model. A few optical fibers from Opsens for thermal measurements are set to the chips, baseplate, heat sink, and the air channel in the heat sink to monitor several critical temperature nodes in the thermal

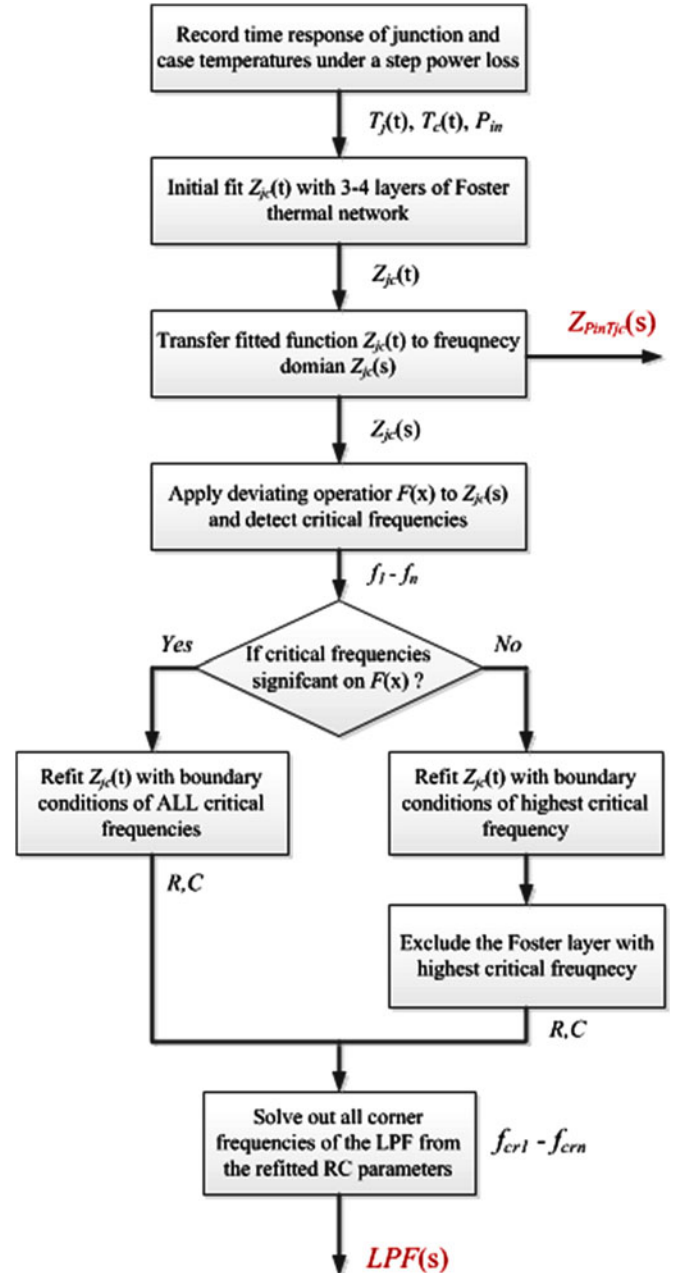

 Fig. 20. Identified corner-frequencies from bode plot of $Z_{P_{in}T_{jc}}$ in Fig. 19.

 Fig. 22. Extracted heat-gain $G_{P_{in}P_{out}}$ from Fig. 21.

 Fig. 21. Extract the insignificant critical frequency f_1 from Fig. 20.

networks, as illustrated in Fig. 17, where a 1-mm depth of gap is curved on the baseplate of module and a 1-mm-diameter hole is drilled into the heat sink for the mounting of sensors. The measuring point for the junction node is in the center of a MOSFET chip, and the rest of measured nodes are all allied in the heat path right beneath the chip of the module. The optical sensor has a measurement range of $-40\text{ }^{\circ}\text{C}$ to $+250\text{ }^{\circ}\text{C}$ with an accuracy of ± 0.3 to $0.8\text{ }^{\circ}\text{C}$, and the response time is limited to 5 ms.

Then, the target MOSFET chip is turned OFF with constant current of 20 A and conduction voltage of 1.315 V, which is equivalent to a step power-loss of 26.3 W applied to the thermal networks of the power module. The junction temperature T_j , case temperature T_c , heat-sink temperature T_h , and ambient temperature T_a are recorded in the time span of 15 s, as shown in Fig. 18. Because the conduction voltage of device is not constant during the turn-on process, actually the voltage at the instant of turning OFF is measured, and then a mathematical transformation is applied to the recorded waveforms to make the temperatures rise along with the time.

A. Characterization of Thermal Behaviors under Frequency Domain

By initially fitting the measured temperature difference of T_j and T_c with the functions shown in (5), the four-layer Foster-type thermal network for the power module can be established, and the RC parameters are shown in Table III. As a result, the


 Fig. 23. Flow chart to acquire $Z_{P_{in}T_{jc}}(s)$ and LPF(s) in Fig. 14.

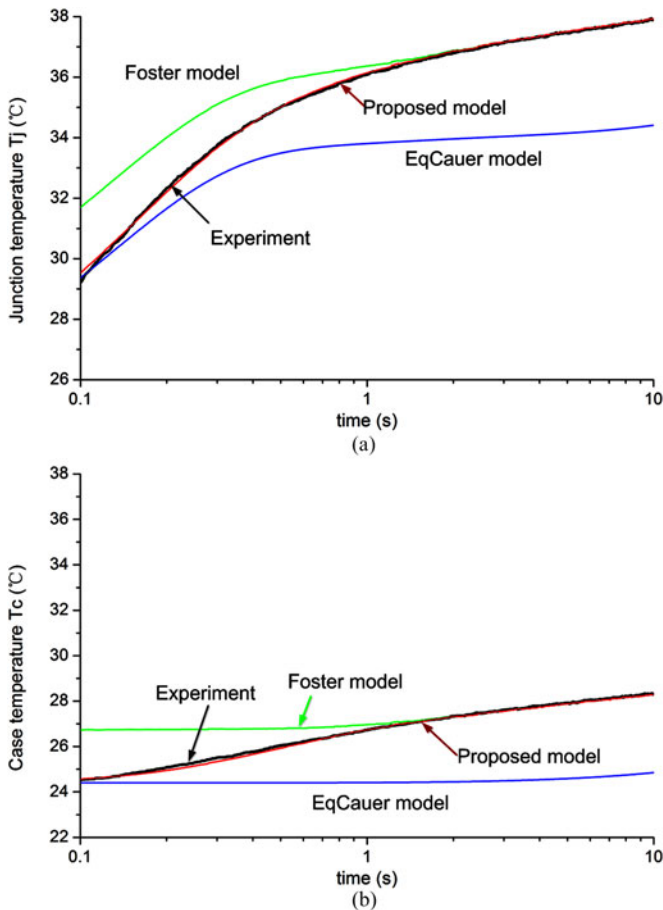


Fig. 24. Comparison of the estimated temperatures of device by various thermal models (the measured T_H is set as reference temperature). (a) Junction temperature T_j . (b) Base-plate temperature T_c .

frequency-domain thermal impedance $G_{P_{in}T_{jc}}$ for the measured power module is plotted in Fig. 19.

By deviating the slope of $Z_{P_{in}T_{jc}}$, the critical-frequencies on the $Z_{P_{in}T_{jc}}$ can be identified, as shown in Fig. 20. It is noted that only two critical frequencies are seen in the experimental results, because the response time of the sensor is limited at 5 ms, which corresponds to a cut-off frequency around 30 Hz, and this will filter out many high-frequency behaviors.

Another important discovery from Fig. 20 is that the critical frequency f_1 is not so significant to be accurately identified; this is mainly because the thermal resistance at this band is much smaller than the one around f_2 , based on the function (14). The solution to this problem is to set only one critical frequency f_2 as boundary condition for the fitting algorithm, with undetermined numbers of RC layers. After refitting $Z_{P_{in}T_{jc}}(s)$, the new foster network should contain one layer (referred as $Z_{f2}(s)$) that represents the corner frequency of f_{cr2} in the heat-gain and corresponding thermal resistance. Afterwards, the rest of the critical frequencies in $Z_{P_{in}T_{jc}}(s)$ can be more accurately identified by analyzing the function of $Z_{P_{in}T_{jc}}(s) - Z_{f2}(s)$, which excludes the behaviors of $Z_{f2}(s)$, as illustrated in Fig. 21.

By refitting the frequency behaviors of $Z_{P_{in}T_{jc}}$ with a new Foster thermal network, and setting the boundary conditions of the numbers and ranges of critical frequency f_1 and f_2 to

the fitted RC pairs, the corner frequencies for the LPF of the power-loss can be extracted, in this case $f_{cr1} = 0.379$ and $f_{cr2} = 1.452$, and the $G_{P_{in}P_{out}}$ of the power module can be plotted in Fig. 22.

As a summary, the flow chart to extract the proposal new thermal model is shown in Fig. 23, where the inputs and outputs of the process are demonstrated.

B. Comparison of the Thermal Models

The experimentally recorded junction temperature T_j and case temperature T_c , as well as the estimated temperatures by using various thermal networks are shown in Fig. 24(a) and (b), respectively, where the heat-sink temperature by experiment is used as the reference temperature for the models. It is noted that the response time of the temperature sensors is limited to 5 ms, making the step response of thermal dynamics below 0.1 s slower than the actual value; and therefore, only the thermal dynamics above 0.1 s is shown and used for the analysis. As it can be seen, the experimental results agree well with the simulations shown in Figs. 8 and 16: The proposed thermal model can not only correctly reflect the thermal behaviors of the temperatures inside the power device, but also has a good agreement with the thermal behaviors outside the power devices, which is hard to be achieved by the existing Foster and its equivalent Cauer thermal networks.

V. CONCLUSION

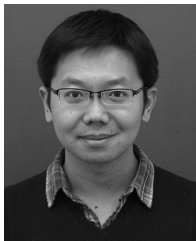
Frequency-domain modeling is conducted on several typically used thermal networks for power semiconductor devices. It is found that either the widely used Foster type or its equivalent Cauer-type thermal networks have their limits to correctly predict the device temperatures, especially when considering the cooling conditions outside the device. The main reason is due to the incorrect heat behavior flowing out of the device.

A new thermal model is proposed in this paper, which put more efforts to establish a correct transfer function for the filtering effects of the power-loss. It is only based on the information of Foster-type thermal network, which is easily accessible from the datasheet or external measurements, and it is independent of the internal materials and structure information of devices. Compared to the existing thermal models, the proposed model can achieve a more correct estimation of the device temperature, when considering the cooling conditions.

REFERENCES

- [1] F. Blaabjerg and K. Ma, "Future on power electronics for wind turbine systems," *IEEE J. Emerg. Sel. Topics Power Electron.*, vol. 1, no. 3, pp. 139–152, Sep. 2013.
- [2] S. Faulstich, P. Lyding, B. Hahn, and P. Tavner, "Reliability of offshore turbines—identifying the risk by onshore experience," presented at the European Offshore Wind Conf. Exhib., Stockholm, Sweden, Sep. 2009.
- [3] B. Hahn, M. Durstewitz, and K. Rohrig, "Reliability of wind turbines – Experience of 15 years with 1500 WTs," in *Wind Energy*. Berlin, Germany: Springer-Verlag, 2007.
- [4] E. Wolfgang, L. Amigues, N. Seliger, and G. Lugert, "Building-in Reliability into power electronics systems," *World Electron. Packag. Syst. Integr.*, pp. 246–252, 2005.
- [5] K. Ma, M. Liserre, F. Blaabjerg, and T. Kerekes, "Thermal loading and lifetime estimation for power device considering mission profiles in wind

- power converter," *IEEE Trans. Power Electron.*, vol. 30, no. 2, pp. 590–602, Feb. 2015.
- [6] J. Due, S. Munk-Nielsen, and R. Nielsen, "Lifetime investigation of high power IGBT modules," in *Proc. Eur. Conf. Power Electron. Appl.*, Birmingham, U.K., 2011, pp. 1–8.
 - [7] A. Wintrich, U. Nicolai, and T. Reimann, *Semikron Application Manual*, p. 128, 2011.
 - [8] J. Berner, *Load-cycling Capability of HiPak IGBT Modules*, ABB Application Note 5SYA 2043-02, 2012.
 - [9] U. Scheuermann, "Reliability challenges of automotive power electronics," *Microelectron. Rel.*, vol. 49, nos. 9–11, pp. 1319–1325, 2009.
 - [10] U. Scheuermann and R. Schmidt, "A new lifetime model for advanced power modules with sintered chips and optimized Al wire bonds," in *Proc. Power Convers. Intell. Motion*, 2013, pp. 810–818.
 - [11] C. Busca, R. Teodorescu, F. Blaabjerg, S. Munk-Nielsen, L. Helle, T. Abeyasekera, and P. Rodriguez, "An overview of the reliability prediction related aspects of high power IGBTs in wind power applications," *Microelectron. Rel.*, vol. 51, nos. 9–11, pp. 1903–1907, 2011.
 - [12] S. Yang, A. Bryant, P. Mawby, D. Xiang, L. Ran, and P. Tavner, "An industry-based survey of reliability in power electronic converters," *IEEE Trans. Ind. Appl.*, vol. 47, no. 3, pp. 1441–1451, May/Jun. 2011.
 - [13] M. Marz and P. Nance, *Thermal Modeling of Power Electronic System*, Infineon Application Note, Munich, Germany, 2000.
 - [14] Infineon Application Note: Thermal Resistance Theory and Practice, Jan. 2000.
 - [15] Infineon Application Note AN2008–03 Thermal equivalent circuit models, Jun. 2008.
 - [16] ABB Application Note: Applying IGBTs, May 2007.
 - [17] ABB Application Note 5SYA 2093-00 Thermal design and temperature ratings of IGBT modules," 2012.
 - [18] Y. C. Gerstenmaier, W. Kiffe, and G. Wachutka, "Combination of thermal subsystems modeled by rapid circuit transformation," in *Proc. Thermic*, 2007, pp. 115–120.
 - [19] Y. Yang, R. Master, G. R. Ahmed, and M. Touzelbaev, "Transient frequency-domain thermal measurements with applications to electronic packaging," *IEEE Trans. Compon. Packag. Manuf. Technol.*, vol. 2, no. 3, pp. 448–456, Mar. 2012.
 - [20] Z. Wang and W. Qiao, "An online frequency-domain junction temperature estimation method for IGBT modules," *IEEE Trans. Power Electron.*, vol. 30, no. 9, pp. 4633–4637, Sep. 2015.
 - [21] B. Du, J. L. Hudgins, E. Santi, S. Member, A. T. Bryant, P. R. Palmer, and H. A. Mantooth, "Transient electrothermal simulation of power semiconductor devices," *IEEE Trans. Power Electron.*, vol. 25, no. 1, pp. 237–248, Jan. 2010.
 - [22] N. Rinaldi, "On the modeling of the transient thermal behavior of semiconductor devices," *IEEE Trans. Electron. Devices*, vol. 48, no. 12, pp. 2796–2802, Dec. 2001.



Ke Ma (S'09-M'11) received the B.Sc. and M.Sc. degrees in electrical engineering from the Zhejiang University, Hangzhou, Zhejiang, China, in 2007 and 2010, respectively, and the Ph.D. degree from the Aalborg University, Aalborg, Denmark, in 2013.

He was a Postdoctoral Researcher with Aalborg University in 2013, where he became an Assistant Professor in 2014. His current research interests include the power electronics and reliability in the application of renewable energy systems.

Dr. Ma serves as an Associate Editor for the IEEE TRANSACTIONS ON INDUSTRY APPLICATIONS. He received the Excellent Young Wind Doctor Award 2014 by European Academy of Wind Energy, and a few prized paper awards by the IEEE.



Ning He (S'15) was born in Zhejiang, China, in 1986. He received the B.S. degree in electrical engineering from the Department of Electrical Engineering, Zhejiang University, Hangzhou, China, in 2009, where he is currently working toward the Ph.D. degree.

From 2014 to 2015, he was supported by the China Scholarship Council to visit and work with the Department of Energy Technology, Aalborg University, Denmark. His research interests include current control, PV generation systems, and soft-switching techniques.



Marco Liserre (S'00–M'02–SM'07–F'13) received the M.Sc. and Ph.D. degree in electrical engineering from the Bari Polytechnic, Orabona, Bari, Italy, in 1998 and 2002, respectively.

He was an Associate Professor with the Bari Polytechnic and Professor in reliable power electronics at Aalborg University, Denmark). He is currently a Full Professor and the Chair of Department of Power Electronics, Christian–Albrechts University of Kiel, Kiel, Germany. Dr. Liserre has published more than 200 technical papers (more than 60 of them in inter-

national peer-reviewed journals), four chapters of a book and a book ("Grid Converters for Photovoltaic and Wind Power Systems," IEEE–Wiley, second reprint). His works have received more than 12000 citations. He is listed in ISI Thomson report "The world's most influential scientific minds," in 2014. He has received the ERC Consolidator Grant for an overall budget of 2 million Euro for the project "The Highly Efficient and Reliable Smart Transformer (HEART), a new Heart for the Electric Distribution System." He is the Member of IAS, PELS, PES, and IES. He is an Associate Editor of the IEEE TRANSACTIONS ON INDUSTRIAL ELECTRONICS, IEEE INDUSTRIAL ELECTRONICS MAGAZINE, IEEE TRANSACTIONS ON INDUSTRIAL INFORMATICS, where he is currently Co-Eic, IEEE TRANSACTIONS ON POWER ELECTRONICS and IEEE JOURNAL OF EMERGING AND SELECTED TOPICS IN POWER ELECTRONICS. He has been the Founder and Editor-in-Chief of the IEEE Industrial Electronics Magazine. He is the Founder and the Chairman of the Technical Committee on Renewable Energy Systems, cochairman of the International Symposium on Industrial Electronics, IES Vice-President responsible of the publications. He has received the IES 2009 Early Career Award, the IES 2011 Anthony J. Hornfeck Service Award, the 2014 Dr. Bimal Bose Energy Systems Award, the 2011 Industrial Electronics Magazine best paper award, and the Third Prize paper award by the Industrial Power Converter Committee at ECCE 2012. He is a Senior Member of IES AdCom.



Frede Blaabjerg (S'86–M'88–SM'97–F'03) received the Ph.D. degree from Aalborg University, Aalborg, Denmark, in 1992.

He was an Assistant Professor in 1992, an Associate Professor in 1996, and a Full Professor of power electronics and drives in 1998. From 1987 to 1988, he was with ABB–Scandia, Randers, Denmark. He is currently a Full Professor with the Department of Energy Technology, Aalborg University. His current research interests include power electronics and its applications such as in wind turbines, PV systems, reliability, harmonics and adjustable speed drives.

Dr. Blaabjerg has received 15 IEEE Prize Paper Awards, the IEEE PELS Distinguished Service Award in 2009, the EPE–PEMC Council Award in 2010, the IEEE William E. Newell Power Electronics Award 2014, and the Villum Kann Rasmussen Research Award 2014. He was an Editor-in-Chief of the IEEE TRANSACTIONS ON POWER ELECTRONICS, from 2006 to 2012. He has been a Distinguished Lecturer for the IEEE Power Electronics Society from 2005 to 2007, and for the IEEE Industry Applications Society from 2010 to 2011.